# On mechanical damping of cantilever beam-based electromagnetic resonators

# On mechanical damping of cantilever beam-based electromagnetic resonators

Faruq Muhammad Foong[1], Thein Chung Ket*[,1], Daniil Yurchenko[2]

[1]School of Engineering and Physical Sciences, Heriot-Watt University, No. 1, Jalan Venna P5/2, Precinct 5, 62200 Malaysia
[2] School of Engineering and Physical Sciences, Heriot-Watt University, Edinburgh EH14 4AS, United Kingdom
*c.thein@hw.ac.uk

**Abstract**

Often when optimising a vibration energy harvester, the mechanical damping is given little significance and is usually assumed to be constant. This paper analyses the importance of mechanical damping variation in modelling the behaviour of a cantilever beam-based electromagnetic resonator. It is shown that for beam volumes above 100 $mm^3$, material damping dominates thermoelastic and air damping, hence becoming the major contributor towards the mechanical damping. A novel method is proposed to define material damping in terms of the maximum critically damped stress at resonance. The new method is shown to be simpler and more accurate than previous methods. Using the developed governing equations, the conditions of optimum load resistance are derived for unique cases. A comparison is made between the mechanical damping model and the constant mechanical damping assumption in terms of maximum power output. It is found that not only are large errors detected when using the constant mechanical damping assumption, but the trending curves were also different. Further analysis suggests that there exists an optimum mass ratio and the conditions for this optimum value are derived for some unique cases. Lastly, this paper compares the maximum power output of an electromagnetic resonator under two common frequency tuning methods. It is shown that different frequency tuning methods are preferable under different conditions.

*Keywords*: Mechanical damping, Cantilever beam, Electromagnetic resonator, Stress, Frequency tuning.

## 1. Introduction

In the mid-90s, William and Yates [1] proposed the concept of vibration energy harvesting as a viable source of sustainable energy to power small electronics. Research in this area has then drastically been increased over the past decade. There exist several methods to convert mechanical vibrations into electrical power, with the two most common methods being electromagnetic induction and piezoelectric conversion. Piezoelectric conversion method is usually the preferred option due to its high power output at small volumes [2]. However, electromagnetic induction method was shown to be better than piezoelectric for device volume higher than 500 $mm^3$ [3]. Beeby et al. [4] demonstrated that if a detailed optimisation was perform, the power output of an electromagnetic resonator can surpass a piezoelectric resonator at a volume of 100 $mm^3$.

The dynamics of a vibrating structure is usually characterised based on its natural frequency and damping capacity. While thorough studies and numerous analytical methods have been conducted on the natural frequency of a structure [5,6], little is known about damping despite its significance. For cases of cantilever beam-based electromagnetic resonators, there are two sources of damping which are the mechanical damping of the beam and the electromagnetic damping due to induced magnetic field [7]. Normally, the mechanical damping of the beam is obtained experimentally as no analytical methods exist to predict this damping. However, the electromagnetic damping can be estimated analytically [8]. Application wise, cantilever beam-based resonators are usually optimised experimentally [9] or by assuming a constant mechanical damping in an analytical optimisation algorithm [10,11]. Currently, the most common method to determine the mechanical damping of a structure is the logarithmic decrement method and the half-power bandwidth method [12]. However, these methods are purely experimental.

The mechanical damping in a common cantilever beam-based resonator design is generally the sum of three damping components which are the material damping, air damping and thermoelastic damping [13]. Although other components of mechanical damping exist, the three mentioned components are the most common source of mechanical damping for cantilever beam-based applications. Material damping arises from the atomic arrangement of the beams as well as its impurities. Hence, material damping is a type of microscopic damping as it exists at a molecular level. Due to this, different materials have different damping properties. In an earlier study, Lazan [14] proposed in his work that a strong relationship exists between the stress experienced in a vibrating structure and the

energy dissipated by the structure (damping energy). His study focused on material damping and he showed that different damping-stress curves exist for different materials. With this, Lazan developed a generalised damping-stress equation for most metals, relating the loss factor of a metallic material to its maximum bending stress and its fatigue limit stress. Kume et al. [15] refined Lazan's damping-stress equation by considering the stress contours in a cantilever and derived a new damping-stress relation, although the results of their equation are very similar to Lazan's. Gounaris and Anifantis's [16] applied the same approach in finite element analysis to analytically determine the material damping of a beam-like structure. Nevertheless, all of these methods are related to the same damping-stress equation and may not be entirely accurate due to the generalisation of the equation [17]. In addition, there were no evidences that the methods presented were valid for beams with tip mass applications. Edberg [18] showed that for small damping ratios, the product of the beam eigenvalue squared and the damping ratio is a constant. However, this theory did not take into account the effects of the forcing input applied to vibrate the beam. To this day, there has been no exact analytical approach to predict the material damping of cantilever beams.

Zener [19] described thermoelastic damping as a form of the energy losses due to the temperature gradient generated by the repeated state of tension and compression in a vibrating beam. Several studies have then recorded the significance of this damping as the main contributor to the mechanical damping in micro-sized structures [20–22]. However, Alblas [23] deemed this form of damping to be negligible in macro-sized structures. Many authors have researched on the importance of ambient air damping due to air drag on the vibration of a cantilever beam [24–26]. Similar to the thermoelastic damping, this form of damping is more significant in the micro-sized region as compared to the macro-size region. Nevertheless, an analytical approach exist to predict both the thermoelastic and air damping of cantilever beam structures. Iourtchenko et al. [27] took the approach to identify the overall damping of a vibrating structure based on the velocity of the structure at resonance. The method considers a single degree of freedom (SDOF) model where the damping parameter is assumed to be an unknown odd function of the velocity at resonance. By applying Schlomilch's integral to the steady-state solution for a slowly varying amplitude and phase, an analytical equation for the unknown damping can be derived. However, velocity if not a unique parameter of damping. This means that if a damping-velocity relation was formed for a cantilever beam with a specific tip mass, it would not be applicable for other tip masses although the same beam properties and size were used, due to the inertial effect of the different tip mass Nevertheless, the damping-velocity relation of a material for a specific tip mass (or even no tip mass) can be applied for any beam size, suggesting that this relation is only a function of the tip mass inertial term.

This study focused on the analysis of mechanical damping for macro-sized cantilever beam-based electromagnetic resonators as significant applications of this resonators lies in the macro range (>100 $mm^3$). The equations of motion for cantilever beams with tip mass were derived based on the Euler-Bernoulli beam theory as the geometry of beams used in resonators are usually slender enough to allow neglecting the effects of shear deformation. An analysis was then performed to determine the significance of each damping component of the mechanical damping in macro scale analysis. A method was then proposed to predict the unknown material damping of cantilever beams base on the hysteretic damping model. A comparison was made between the power output of an electromagnetic resonator using the developed mechanical damping model and using the constant mechanical damping assumption. Conditions of certain optimum parameters for unique cases were derived in this work. Finally, a discussion was made on the preferred method of frequency tuning for electromagnetic resonators.

## 2. Governing equations

To fully model the behaviour of a cantilever beam-based electromagnetic resonator, the following equations are required:

- Cantilever beam equation of motion
- Electromagnetic power equation
- Damping equations

This section describes the derivation of the each governing equations as to model the electromagnetic resonator.

### 2.1 Transverse equation of motion of a cantilever beam with a tip mass

Consider cases where a tip mass is placed at the tip of a clamp-free cantilever beam as shown in Figure 1. The tip mass will presume a cuboid shape for simplicity.

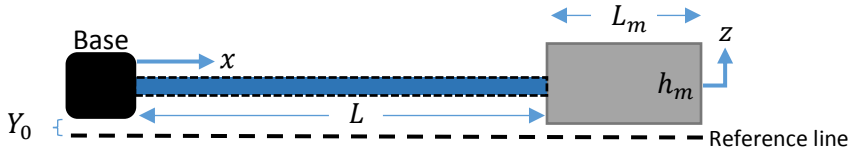


**Figure 1.** Cantilever beam with a tip mass fixed at its free-end.

The transverse motion of the clamp-free cantilever beam subjected to a harmonic-base excitation at position $x$ and time $t$ can be described by the following equation.

$$z_{abs}(x,t) = z_{rel}(x,t) + Y_0(t) \tag{1}$$

where $z_{\text{abs}}(x,t)$ is the absolute vertical displacement of the vibrating beam, $z_{\text{rel}}(x,t)$ is the vertical displacement of the beam relative to its clamped base and $Y_0(t)$ is the vertical amplitude of the base excitation. For simplicity, the base excitation is assumed to be in harmonic motion. Based on the Euler–Bernoulli beam theory, the equation of motion for undamped-free vibrations is given as:

$$EI\frac{d^4 z_{rel}(x,t)}{dx^4} + \rho A\frac{d^2 z_{rel}(x,t)}{dt^2} = 0 \tag{2}$$

where $E$ is the Young's modulus of the beam, $I$ is the second moment of area, $\rho$ is the density and $A$ is the cross sectional area. Using the method of separation of variables, the term $z_{rel}(x,t)$ can be separated into its spatial and temporal components.

$$z_{rel}(x,t) = \sum_{n=1}^{\infty} \varphi_n(x)\eta_n(t) \tag{3}$$

where $\varphi_n(x)$ is the cantilever beam's modal-shape eigenfunction and $\eta_n(t)$ is the regular-response function. Substituting equation (3) into equation (2) results in the following equations

$$\frac{d^4\varphi_n(x)}{dx^4} - {\lambda_n}^4\varphi_n(x) = 0 \tag{4}$$

$$\frac{d^2\eta_n(t)}{dt^2} + {\omega_n}^2\eta_n(t) = 0 \tag{5}$$

where $\omega_n$ is the natural frequency of the beam-mass system and ${\lambda_n}^4$ is defined as

$${\lambda_n}^4 = \frac{\rho A{\omega_n}^2}{EI} \tag{6}$$

By equating $\varphi(x) = e^{\lambda x}$, the homogeneous solution for equation (4) can be derived in the form of

$$\varphi(x) = D_1 cosh\lambda x + D_2 sinh\lambda x + D_3 cos\lambda x + D_4 sin\lambda x \tag{7}$$

where $D_1, D_2, D_3$ and $D_4$ are unknown constants. Assuming that the tip mass is made of a rigid material, the following equations can be deduced.

$$m_b = \rho Lhw \tag{8}$$

$$m_t = \rho_m L_m h_m w_m \tag{9}$$

$$M_S = \frac{m_t L_m}{2} \tag{10}$$

$$I_t = \frac{\left(4{L_m}^2 + {h_m}^2\right)}{12} m_t \tag{11}$$

where $\rho, L, h$ and $w$ represent the density, length, thickness and width parameter of the cantilever beam and the subscript $m$ represents the same parameters for the tip mass. Hence, $m_b$ and $m_t$ defines the mass of the cantilever beam and the tip mass. $M_S$ and $I_t$ is the static mass moment and the rotary inertia contribution of the tip mass acting at the free-end of the beam. It is to emphasise that the rotary inertia representation in equation (11) describes a cuboid shape tip mass and can easily be modified to represent other geometries. The tip mass is assumed to act as a

distributed mass on the beam, where the static mass is considered to act at the centre of the mass. This will result in the boundary conditions for equation (2) to be

$$EI\varphi_n(0) = EI\frac{d\varphi_n}{dx}(0) \tag{12}$$

$$EI\frac{d^2\varphi_n}{dx^2}(L) = {\omega_n}^2\left[I_t\frac{d\varphi_n}{dx}(L) + M_S\varphi_n(L)\right] \tag{13}$$

$$EI\frac{d^3\varphi_n}{dx^3}(L) = -{\omega_n}^2\left[m_t\varphi_n(L) + M_S\frac{d\varphi_n}{dx}(L)\right] \tag{14}$$

Substituting the boundary conditions into equation (7) results in the following matrix.

$$\begin{bmatrix} O_{11} & O_{12} \\ O_{21} & O_{22} \end{bmatrix}\begin{bmatrix} D_1 \\ D_2 \end{bmatrix} = \begin{bmatrix} 0 \\ 0 \end{bmatrix} \tag{15}$$

where

$$O_{11} = cosh\beta_n + cos\beta_n - \frac{{\beta_n}^3 I_t}{m_b L^2}(sinh\beta_n + sin\beta_n) - \frac{{\beta_n}^2 M_s}{m_b L}(cosh\beta_n - cos\beta_n) \tag{16}$$

$$O_{12} = sinh\beta_n + sin\beta_n - \frac{{\beta_n}^3 I_t}{m_b L^2}(cosh\beta_n - cos\beta_n) - \frac{{\beta_n}^2 M_s}{m_b L}(sinh\beta_n - sin\beta_n) \tag{17}$$

$$O_{21} = sinh\beta_n - sin\beta_n + \frac{\beta_n m_t}{m_b}(cosh\beta_n - cos\beta_n) + \frac{{\beta_n}^2 M_s}{m_b L}(sinh\beta_n + sin\beta_n) \tag{18}$$

$$O_{22} = cosh\beta_n + cos\beta_n + \frac{\beta_n m_t}{m_b}(sinh\beta_n - sin\beta_n) + \frac{{\beta_n}^2 M_s}{m_b L}(cosh\beta_n - cos\beta_n) \tag{19}$$

where $\beta_n = \lambda_n L$. By equating the determinant of equation (15) to zero, the frequency constant, $\beta$, corresponding to the $n^{th}$ mode of vibrations can be determined. The natural frequency of the beam can then be calculated using equation (20).

$$\omega_n = {\beta_n}^2\sqrt{\frac{Eh^2}{12\rho L^4}} \tag{20}$$

Therefore, the eigenfunction of the beam for the $n^{th}$ mode shape is

$$\varphi_n(x) = D_2\left[cosh\frac{\beta_n}{L}x - cos\frac{\beta_n}{L}x - \frac{O_{21}}{O_{22}}\left(sinh\frac{\beta_n}{L}x - sin\frac{\beta_n}{L}x\right)\right] \tag{21}$$

Equation (21) is identical to the equation developed in some literatures [28,29], where unknown $D_2$ can be found by normalisation. The response of the beam was then determined from its effective mass and the forcing vector. In this study, the approach developed by Erturk and Inman [30] was used to solve for $D_2$ as it is simpler. Here, the orthogonality conditions must be considered.

$$\frac{m_b}{L}\int_0^L[\varphi_n(x)]^2dx + \varphi_n(L)\left[m_t\varphi_n(L) + M_S\frac{d\varphi_n}{dx}(L)\right] + \frac{d\varphi_n}{dx}(L)\left[I_t\frac{d\varphi_n}{dx}(L) + M_S\varphi_n(L)\right] = 1 \tag{22}$$

$$L\int_0^L[\varphi_n(x)]^2dx - \varphi_n(L)EI\frac{d^3\varphi_n}{dx^3}(L) + \frac{d\varphi_n}{dx}(L)EI\frac{d^2\varphi_n}{dx^2}(L) = {\omega_n}^2 \tag{23}$$

By solving equations (22) or (23), the value of $D_2$ can be determined. For a steady-state solution, a simple single-degree-of-freedom model can be used to represent the temporal term $\eta_n(t)$.

$$\ddot{\eta_n}(t) + 2\zeta_n\omega_n\dot{\eta_n}(t) + {\omega_n}^2\eta_n(t) = -m\omega^2 Y_0 e^{i\omega t}F_n \tag{24}$$

where $\zeta_n$ is the modal mechanical damping ratios of the cantilever beam and $F_n$ is the forcing function described by

$$F_n = \frac{m_b}{L}\int_0^L\varphi_n(x)dx + m_t\varphi_n(L) + M_S\frac{d\varphi_n}{dx}(L) \tag{25}$$

Equation (24) can be solved with reference to the solution for the general SDOF vibration model. The solution for equation (24) is

$$\eta_n(t) = \frac{Y_0 e^{i\omega t}F_n}{{\omega_n}^2 - \omega^2 + i2\zeta_n\omega_n\omega} \tag{26}$$

Substituting equations (21) and (26) into equation (3) and considering only the first mode parameters at resonance ($\omega = \omega_1$) results in

$$z_{rel}(x,t) = \frac{Y_0 e^{i\omega_1 t}\varphi_1(x)}{2\zeta_1} F_1 \tag{27}$$

To evaluate the relative motion of the beam when $x > L$, it is sufficient to assume that the deflection curve of the beam behaves linearly after $x = L$. Therefore, the relative motion for this case is

$$z_{rel}(x > L, t)_{max} = z_{rel}(L,t) + L_m sin\left\{tan^{-1}\left[\frac{z_{rel}(L,t)}{\varphi_1(L)}\frac{d\varphi_1}{dx}(L)\right]\right\} \tag{28}$$

Euler-Bernoulli's theory state that the bending stress of a cantilever beam can be approximated by

$$\sigma = Ey\frac{d^2 z_{rel}(x)}{dx^2} \tag{29}$$

where $\sigma$ is the stress experienced on the beam and $y$ is the distance from the centre of the beam along the thickness. Substituting equation (27) into equation (28) and evaluating the stress value at $x = 0$ defined the maximum bending stress acting on the vibrating beam results in an expression describing the maximum stress of a vibrating beam for the first mode of vibrations

$$\sigma_{max} = E\frac{h}{2}\frac{Y_0}{\zeta_1}\left(\frac{\beta_1}{L}\right)^2 D_2 F_1 \tag{30}$$

### 2.2 Electromagnetic power equation

Figure 2 below describes the schematic of a typical electromagnetic circuit. The coil and the load resistance are defined by $R_c$ and $R_L$ respectively.

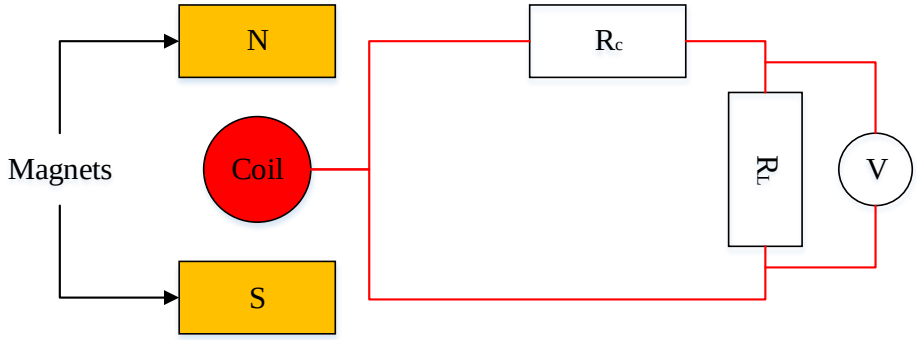


**Figure 2.** Schematic of a general electromagnetic circuit.

Based on Faraday's law of electromagnetic induction and Kirchhoff's voltage law, the voltage is:

$$V_L = NBL_c v_c C\frac{R_L}{(R_c+R_L)} \tag{31}$$

where $V$ is the voltage across the load resistance, $N$ is the number of turns of coil, $B$ is the strength of the magnetic field, $L_c$ is the operative length of the coil, $v_c$ is the relative cutting speed of the coil moving through the magnetic field, $C$ is the coil fill factor [8]. Applying Ohm's law, the power output at the load resistance is

$$P = (NBL_c v_c C)^2\frac{R_L}{(R_c+R_L)^2} \tag{32}$$

In a cantilever beam-based electromagnetic vibration energy harvester, the coil or the magnets is usually attached to the free-end beam at $x = L$. Assuming that $v_c$ is equal to the maximum free-end velocity of the vibrating beam and considering the effects of electromagnetic damping,

$$v_c = \omega_1\frac{Y_0\varphi_1(L)}{2(\zeta_1+\zeta_e)}F_1 \tag{33}$$

where $\zeta_e$ is the electromagnetic damping. It is easy to notice that $v_c$ is simply the derivative of equation (27) with respect to time at $x = L$. In addition, it is also possible to extrapolate $v_c$ using equation (28) to obtain velocities beyond $x = L$. Therefore, the average maximum power of the harvester is

$$P_{max} = (NBL_c\omega_1 Y_0 \varphi_1(L) F_1 C)^2 \frac{R_L}{8(\zeta_1+\zeta_e)^2(R_c+R_L)^2} \tag{34}$$

The derived governing equations present a complete model that describes the behaviour of an electromagnetic harvester. However, the equations defining the variation of electromagnetic damping and mechanical damping have yet to be modelled.

### 2.3. Damping equations

Generally, an electromagnetic cantilever beam-based resonator contains two sources of damping, which are the electromagnetic damping and the mechanical damping. The electromagnetic damping arises from the interaction between the induced current in the coil and the magnetic field due to a change in the magnetic flux. This results in the generation of an electromotive force that retards movement. The magnitude of this form of damping can be described by equation (35) [8]

$$\zeta_e = \frac{(NBL_cC)^2}{2m_e\omega_1(R_c+R_L)} \tag{35}$$

where $m_e$ is the effective mass of the electromagnetic resonator. It was discussed earlier on the characteristic of mechanical damping in where the damping is material specific. In general, mechanical damping of a cantilever beam is the sum of three different types of damping:

$$\zeta_1 = \zeta_m + \zeta_h + \zeta_a \tag{36}$$

where $\zeta_m$ is the material damping, $\zeta_h$ is the thermoelastic damping and where $\zeta_a$ is the air damping contribution. This section presents a new method to develop simple damping-stress equations from experiment results to address the material damping of cantilever beams. In this study, the material damping-stress equation for a 1050A aluminium material was developed. Since this method was formulated assuming a simple hysteretic loop behaviour, the method presented here can be applied to any material and geometry that resembles this behaviour.

#### 2.3.1 Thermoelastic and air damping

The effect of compression and expansion in a vibrating structure causes a temperature gradient that results in the loss of internal energy. Zener [19] described this loss as a form of damping, namely thermoelastic damping. Zener then proposed a model relating the thermoelastic damping to the thermal properties and driving frequency of the vibrating beam. Assuming proportional damping where the damping ratio is equal to half of the loss factor [31], the expression for the thermoelastic damping is given by

$$\zeta_h = \frac{\Delta e}{2}\frac{\omega\tau}{1+(\omega\tau)^2} \tag{37}$$

where $\Delta e$ and $\tau$ are defined as

$$\Delta e = \frac{E\alpha^2 T_0}{\rho C_p} \tag{38}$$

$$\tau = \frac{h^2}{\pi^2 k} \tag{39}$$

The constants $\alpha$, $T_0$, $C_p$ and $k$ corresponds to the material thermal expansion coefficient, ambient temperature, specific heat capacity and material thermal diffusivity. Lifshitz and Roukes [20] improved Zener's equation by developing an exact solution for the thermoelastic damping in rectangular beams as shown in equation (40)

$$\zeta_h = \frac{3\Delta e}{\varepsilon^2}\left[1 - \frac{sinh\varepsilon+sin\varepsilon}{\varepsilon(cosh\varepsilon+cos\varepsilon)}\right] \tag{40}$$

where

$$\varepsilon = h\sqrt{\frac{\omega}{2k}} \tag{41}$$

Although equation (40) was derived while considering micro-cantilever beams, it is also valid for macro cantilever beam applications [32]. Hu et al. [33] proved that equation (40) was also valid for cantilever beams with tip mass. Zhang et al. [24] performed a detailed analysis on the effect of air damping on cantilever beam vibrations. The following equation was proposed to define the air damping factor assuming a moderately laminar airflow.

$$\zeta_a = \frac{4\mu L^2}{wt^2{\beta_n}^2}\sqrt{\frac{3}{\rho E}} \tag{42}$$

where $\mu$ is the viscosity of air which is $1.81 \times 10^{-5}$ Ns/m$^2$. It was emphasised that equation (42) is limited and that an accurate solution for air damping would require a full scale computational analysis. However, equation (42) provides the means of a simple analytical approach for air damping predictions. The significance of both the thermoelastic damping and the air damping on the total mechanical damping was then analysed based on a beam volume for the following material properties of 1050A aluminium listed in Table 1.The ambient temperature was set to be the standard room temperature of $T_0$ = 298 K.

**Table 1.** Material properties of 1050A aluminium.

| Properties | Value |
|---|---|
| $E$ (GPa) | 63 |
| $\rho$ (kgm$^{-3}$) | 2656 |
| $\alpha$ (K$^{-1}$) | $24 \times 10^{-6}$ |
| $C_p$ (Jkg$^{-1}$K$^{-1}$) | 900 |
| $k$ (JK$^{-1}$) | $9.3 \times 10^{-5}$ |

Figure 3 describes the variation in thermoelastic and air damping ratio with a beam volume for different beam aspect ratio, plotted using equations (40) and (42). The beam aspect ratio is defined as the ratio of the beam's length to its thickness. From equation (20), increasing the aspect ratio would decrease the natural frequency of a beam. Volumes above 100 mm$^3$ are considered to lie in the macro region and volumes below that lie in the micro region.

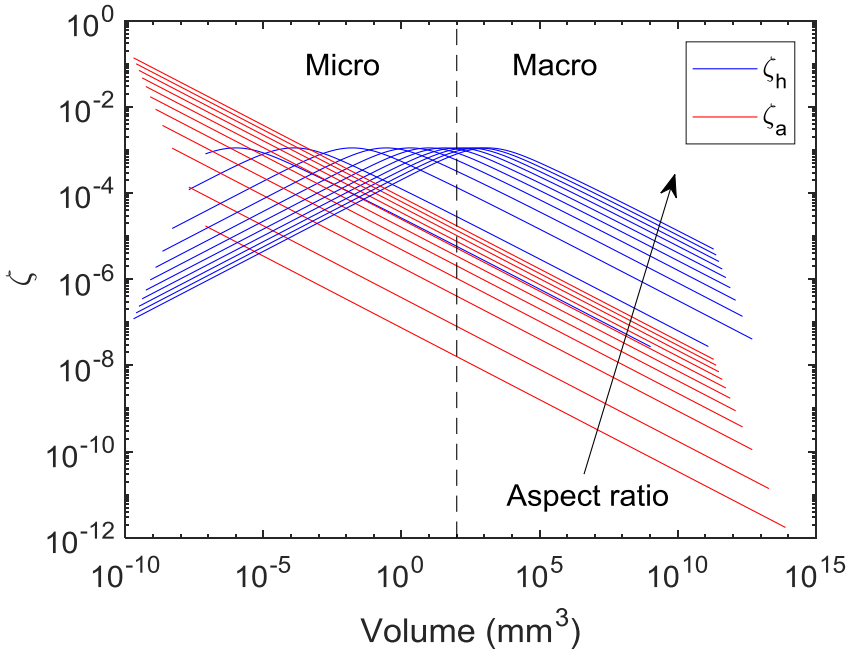


**Figure 3.** Variation in thermoelastic damping (blue) and air damping (red) with beam volume for different beam aspect ratios.

It can be seen that within the macro regions, air damping is very small and can be assumed negligible for all aspect ratios. On the other hand, the significance of thermoelastic damping is dependent on the aspect ratio, in where for low aspect ratio beams, the thermoelastic damping becomes significant in the micro region whereas at higher aspect ratios, thermoelastic damping is significant in the macro regions. Many studies have described the significance of thermoelastic and air damping for micro or nano-sized beam resonators, which is in agreement with the results in

Figure 3. However, this study focuses on analysis in the macro regions of high aspect ratio beams (> 40). Hence, air damping can be ignored but thermoelastic damping may be important, especially for low frequency applications. In addition, this also verifies the application of the Euler-Bernoulli beam theory in this study. Nevertheless, it is shown later that in the macro regions, the thermoelastic damping is much smaller than the material damping for 1050A aluminium. It is arguable that the effect of air damping would increase with the addition of a tip mass. However, Erturk and Inman [34] reported that in this case, the contribution of air damping would actually reduce due to the increase in inertial effects. It is worth to mention that micro-sliding induced damping is also a possible contributor of mechanical damping in cantilever beam-based applications. This form of damping arises from the frictional interaction at the beam-clamp interface. However, this damping is only significant in the micro region [35] and may be significant for macro volumes if screws or joints are used [36].

### 2.3.2 Hysteretic damping model for material damping

Due to the variety of atomic arrangement within materials, different materials exhibit different internal damping capacity. For some materials, the damping capacity was found to be independent of the driving frequency under cyclic stress or vibrations. This type of damping is known as hysteretic damping and is usually related to material damping. In clamp-free cantilever beam vibrations, damping is usually associated with the resonant response of the free-end beam. Therefore, this study applies the hysteretic damping model as frequency-dependent damping models such as Rayleigh damping and viscoelastic damping are out of the scope of this study. Hysteretic damping is often associated with the area encompassed by the loading and unloading state of a stress-strain curve as seen in Figure 4. This area is described as the energy dissipated (damping energy) per unit volume of the structure. The damping capacity of the structure is then measured as the ratio of the damping energy per unit volume to the maximum strain energy stored, otherwise known as the loss factor. Usually, an ellipse shape is presumed for the curve to simplify calculations.

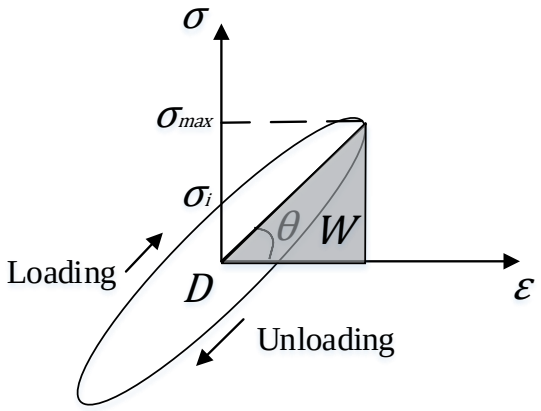


**Figure 4.** Hysteretic damping model.

Assuming a perfect elliptical loop, the damping energy per unit volume, $D$, can be calculated by

$$D = \pi \frac{\sigma_{max}}{sin\theta} \sigma_i cos\theta \tag{43}$$

where

$$E = tan\theta \tag{44}$$

The total stored strain energy represented by the shaded region, $W$, can be described by

$$W = \frac{{\sigma_{max}}^2}{2E} \tag{45}$$

Then

$$\gamma = \frac{D}{2\pi W} = \frac{\sigma_i}{\sigma_{max}} \tag{46}$$

where $\gamma$ is the loss factor of the structure. Assuming proportional damping,

$$\zeta_m = \frac{\sigma_i}{2\sigma_{max}} \tag{47}$$

Equation (30) stated that the maximum bending stress of a vibrating cantilever beam is inversely proportional to its first mode damping ratio. Relating equation (47) to equation (30), this suggest that $\sigma_i$ is independent of the damping parameter and can be defined as

$$\sigma_i = EhY_0 \left(\frac{\beta_1}{L}\right)^2 D_2 F_1 \tag{48}$$

Since $\sigma_i$ is actually related to twice the structure's stress value when $\zeta_1 = 1$, this parameter will we defined as the maximum critically damped stress at resonance. Equation (43) states that $D$ is a function of $\sigma_{max}$ and $\sigma_i$. Previously, Lazan [14] derived a damping-stress equation for metals based on the maximum stress parameter of structures. His experimental analysis displayed a good correlation between the maximum stress and the loss factor of a structure for a single material. Similarly, one could also expect a strong correlation between damping and the maximum critically damped stress in hysteretic damping.

### 2.3.3 Development of material damping-stress equation

An experiment was performed to analyse the damping-stress relation of a 1050A aluminium cantilever beam. Only cases of tip mass were considered as it is more suited to electromagnetic vibration energy harvesting applications. Figure 5 illustrates the schematic diagram of the performed experiment.

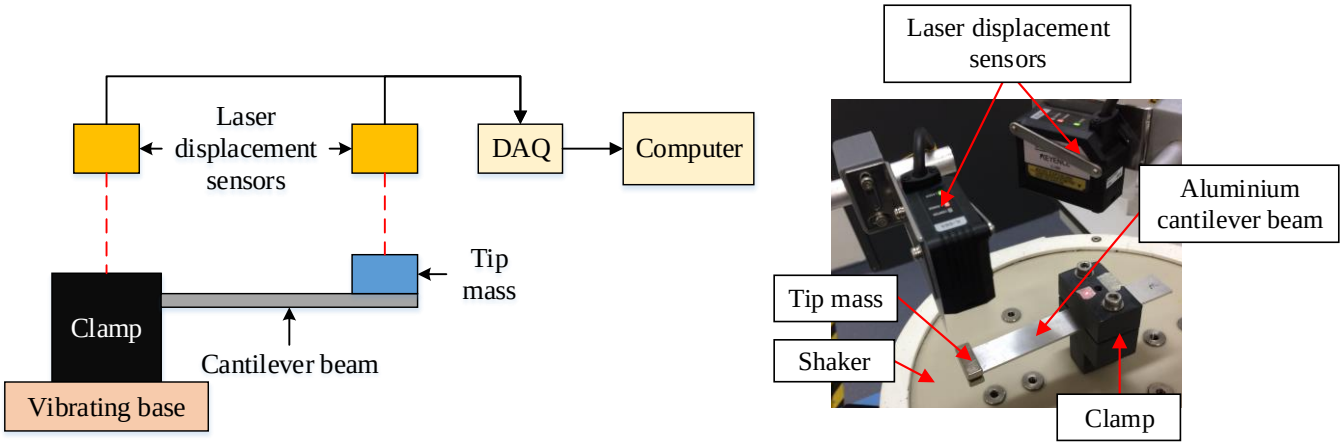


**Figure 5.** Diagram representation (left) and actual (right) of the experimental setup to obtain the mechanical damping of cantilever beams.

The cantilever beam was clamped onto an Espec EV-501 analogue vibration shaker to induce base-excitation motion. The beam was vibrated within a range of frequencies to ensure the occurrence of the first mode resonance. Two laser displacement sensors of model Keyence IL-065 were used to record the response output of the beam and the base. These readings were then sent to a computer for analysis. Full details on the experimental procedure is described in [37]. The experiment was repeated several times using different beam geometry and the tip mass to obtain a variety of stress and damping readings. The beam aspect ratios used varied from 40 to 80 whereas the tip mass varied from 9 grams to 60 grams. Different base excitation accelerations ranging from 0.05 $g$ to 0.6 $g$ (1 $g$ = 9.81 ms$^{-2}$) were also used to obtain different stress levels. To ensure consistency in the damping results, the mechanical damping ratios of each experiment were calculated using equation (28). This value was than subtracted with the thermoelastic damping ratio determined using equation (40) to obtain the material damping ratio. As stated earlier, since this work focuses on macro size resonators, the contribution of air damping is negligible and will not be considered in the experiment. The maximum stress and the maximum critically damped stress were calculated using equations (30) and (48).

Figure 6 describes the experimental results of the overall mechanical damping ratio, $\zeta_1$, and the material damping ratio, $\zeta_m$, plotted against the maximum critically damped stress. Results in Figure 6 shows a very close correlation between the overall mechanical damping ratio and the material damping ratio of 1050A aluminium. This suggest that the thermoelastic damping contributes much less than the material damping in the macro volume regions. Nevertheless, it would be inaccurate to neglect thermoelastic damping in analysis which can contribute up to 15% of the total mechanical damping especially at lower stress levels.

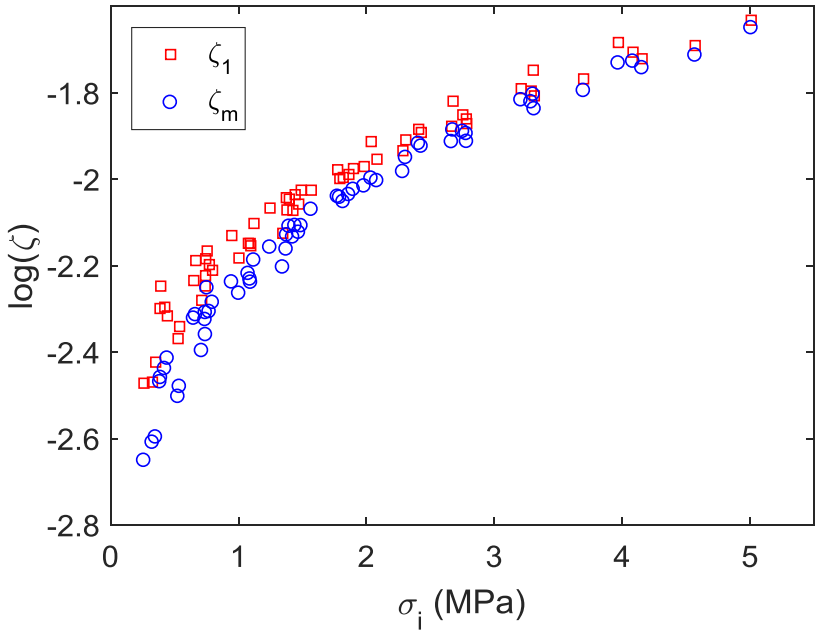


**Figure 6.** Variation in mechanical damping and material damping of 1050A aluminium beam.

The relationship between material damping with the maximum stress and the maximum critically damped stress parameters were then analysed by plotting the experimental mechanical damping results against the respective variables. A best fit curve was fitted to both data as shown in Figure 7.

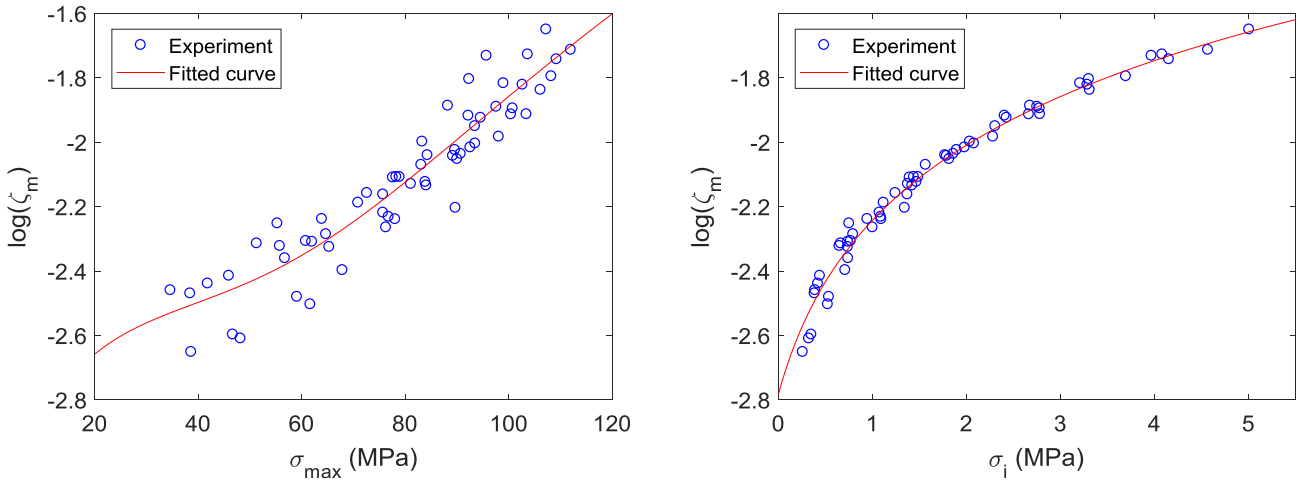


**Figure 7.** Comparison between the correlation of material damping ratio when plotted against maximum stress and maximum critically damped stress.

The quality of the fitted curves were then evaluated based on their root-mean-squared error (RMSE).

$$RMSE = \sqrt{\frac{1}{j}\sum_{1}^{j}(Fitted\ curve - Experiment)^2} \tag{49}$$

The RMSE is a method of evaluating the quality of a fitted curve based on the residual errors. This evaluation method is not normalized and is dependent on the scale of the data. A RMSE value closer to zero indicates a better fit and hence will be more useful for predictions. The RMSE values for Figures 7 (a) and (b) were 0.0018 and 0.0004 respectively. This shows that a better correlation is observed between damping and the maximum critically damped stress as compared to the maximum stress. In addition, the maximum critically damped stress parameter is advantageous in terms of its independence of the damping ratio parameter. Hence, iterations are not required to predict the damping of un-tested samples. Hence, the fitted curve equation from Figure 7 (b) and equation (48) was

used to define the total mechanical damping of 1050A aluminium in further analysis of this work. The final mechanical damping equation is shown below. Here, $\zeta_m$ is defined as a function of $\sigma_i$, $f(\sigma_i)$.

$$\zeta_1 = f(\sigma_i) + \zeta_h \tag{50}$$

## 3. Analytical analysis and discussion

All governing equations required to fully describe the behaviour of a cantilever beam-based electromagnetic resonator have now been modelled. Previous authors have often used the assumption of a constant mechanical damping ratio when modelling or optimising a resonator. To study the implication of this assumption as compared to the mechanical damping ratio model developed in this work, the condition of optimum load resistance must first be addressed.

### 3.1 Optimum load resistance

Often, when working with resonators, the optimum load resistance, ${R_L}^{opt}$, becomes a topic of interest. While some authors argue that ${R_L}^{opt} = R_c$ [38], others believe that ${R_L}^{opt}$ is obtained when $\zeta_e = \zeta_1$ [39]. To analyse the condition of optimum load resistance, the following term is defined

$$M = (NBL_cC)^2 \tag{51}$$

where $M$ will be defined as the magnetisation parameter. Considering the case where $M$ is small and hence $\zeta_e \ll \zeta_1$ for all load resistance input, the total damping of the resonator can then be approximated by

$$(\zeta_1 + \zeta_e) \approx \zeta_1 \tag{52}$$

This reduces equation (34) to

$$P_{max} \approx (\omega_1 Y_0 \varphi_1(L) F_1)^2 \frac{MR_L}{8{\zeta_1}^2(R_c+R_L)^2} \tag{53}$$

Since for a specific resonator parameter the values of $\omega_1$, $Y_0$, $\varphi_1(L)$, $F_1$, $M$ and $\zeta_1$ are constants, the maximum power would depend only on the following parameter

$$P_{max} \propto \frac{R_L}{(R_c+R_L)^2} \tag{54}$$

This parameter is maximised when $R_L = R_c$. Therefore, the condition of optimum load resistance when $M$ is small is $R_L = R_c$. Now consider the case where $M$ is large and $\zeta_e \gg \zeta_1$ at low load resistance value. Re-writing equation (34) results in

$$P_{max} = 2m_e{\omega_1}^3(Y_0\varphi_1(L)F_1)^2 \frac{\zeta_e R_L}{8(\zeta_1+\zeta_e)^2(R_c+R_L)} \tag{55}$$

It is important to notice that $P_{max}$ is highly dependent on the total damping vibrating resonator. Equation (55) states that increasing $R_L$ reduces $\zeta_e$. This in turn would generally increase the overall power output. However, when using high $M$ values, a large load resistance is usually required to significantly reduce the electromagnetic damping and increase the power output, resulting in $R_L \gg R_c$. In this situation, $R_L/(R_c + R_L) \approx 1$ and equation (55) can be reduced to the following

$$P_{max} \approx 2m_e{\omega_1}^3(Y_0\varphi_1(L)F_1)^2 \frac{\zeta_e}{8(\zeta_1+\zeta_e)^2} \tag{56}$$

Removing the constants parameters, the maximum power output would then depend on

$$P_{max} \propto \frac{\zeta_e}{(\zeta_1+\zeta_e)^2} \tag{57}$$

This parameter is maximised when $\zeta_e = \zeta_1$. Figure 8 describes the variation in ${R_L}^{opt}$ with $\zeta_1$ and $\zeta_e$.

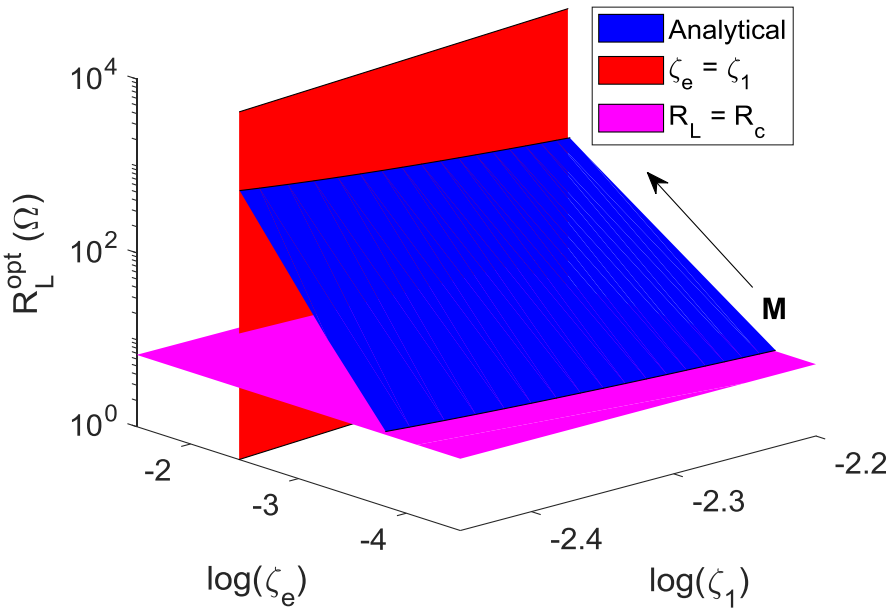


**Figure 8.** Variation in optimum load resistance with electromagnetic damping and mechanical damping.

In Figure 8, the value of $M$ was increased by increasing the magnetic field strength, $B$. Results in Figure 8 suggest that at low $M$ values, the condition of optimum load resistance is $R_L \approx R_c$. However, when $M$ becomes significantly high, the optimum load resistance is achieved when $\zeta_e \approx \zeta_1$. This is in agreement with equations (54) and (57). Between these ranges, the condition for ${R_L}^{opt}$ relates back to equation (34), in where ${R_L}^{opt}$ would then equal to the load resistance value when $\partial P_{max}/\partial R_L = 0$.

### 3.2 Comparison with the constant mechanical damping assumption

The application of the constant mechanical damping ratio assumption in analytical optimisation of a resonator may lead to errors in output predictions. Figure 9 shows the effect of this assumption on the optimum load resistance and its corresponding electrical damping ratio, load voltage and maximum power output of an electromagnetic resonator at different tip mass to beam mass ratios, $m_r$. Hence, plots in Figure 9 all corresponds to the optimum load resistance case. The analysis was conducted under a constant base excitation acceleration input. The mass ratio parameter was used to give a more general insight on the analysis. Case 1 in Figure 9 refers to the actual analytical results where mechanical damping is determined from equation (50) whereas Case 2 corresponds to the constant mechanical damping assumption.

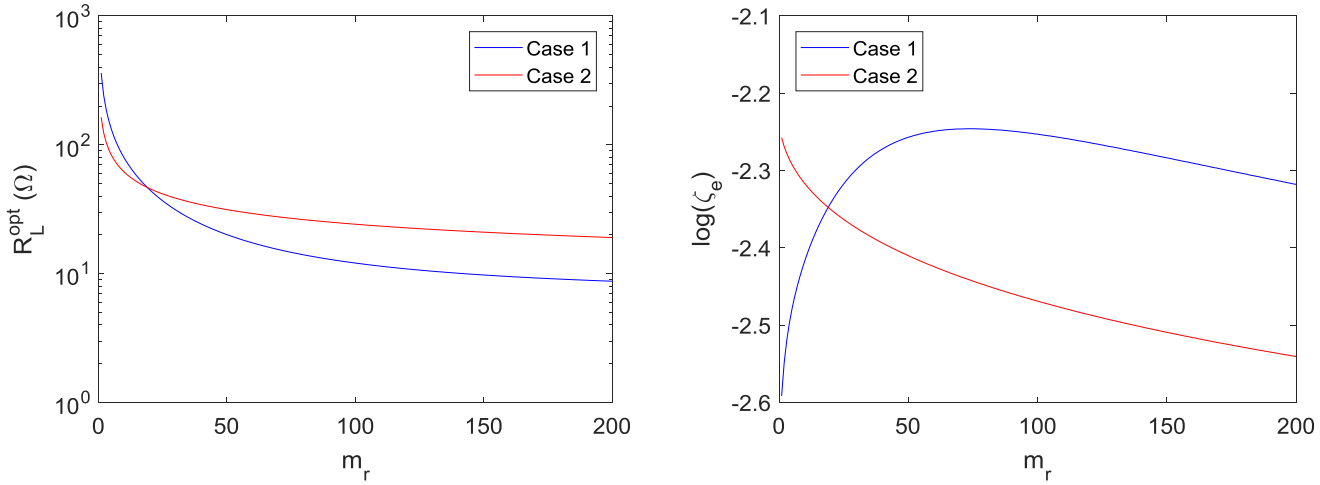

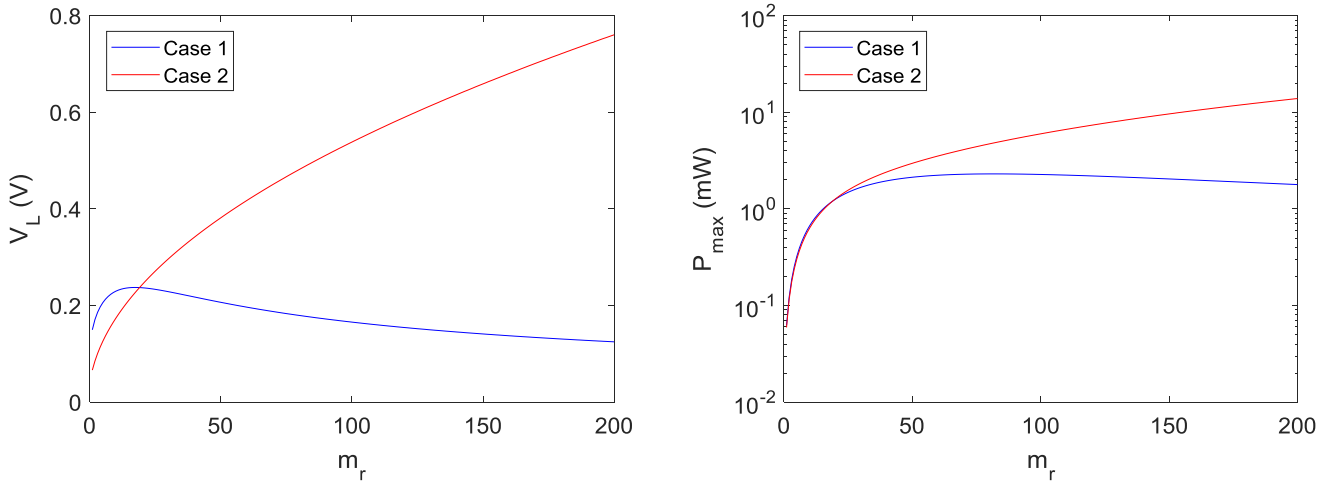


**Figure 9.** Parametric comparison between Case 1 and Case 2.

Results not only show a large error in predictions but also different trends were displayed by the Case 1 and Case 2 for certain parameters. The optimum load resistance curves for both Cases 1 and 2 resulted in a similar trend where ${R_L}^{opt}$ decreases with increasing $m_r$. The predictions on ${R_L}^{opt}$ are also somewhat similar at low $m_r$ values. However, errors can reach up to 100% when dealing with large mass ratios. In addition, most optimisation algorithms would converge to a large mass ratio as its final optimized parameter due to the requirement of low frequency applications and volume constraint [11]. It is worth to note that all the intersections between Case 1 and Case 2 corresponds to when the damping prediction of equation (50) matches the constant mechanical damping input. The electrical damping ratio displayed different trends for Cases 1 and 2. While Case 2 resulted in a decreasing trend for all $m_r$ values, Case 1 showed an increasing trend at low $m_r$ values which shifted to a decreasing trend after a certain mass ratio. A similar trend was also observed for the load voltage plot for Case 1. The most important part of this analysis is the trend in the maximum power output for Cases 1 and 2. The major differences between the two cases in the maximum power prediction is that since Case 2 assumes a constant mechanical damping, the maximum power will continue to increase with increasing mass ratio due to a decrease in natural frequency. On the other hand, Case 1 displayed a possible peak in the curve. Hence, this results in a different definition of power output for Cases 1 and 2. Case 2 suggest that increasing the mass ratio of the resonator would always result in a better power output. However, Case 1 shows that there is an optimum mass ratio value where above this value, the maximum power actually drops with increasing mass ratio. This optimum value is dependent of the mass and geometry of the beam-mass system.

### 3.4 Discussion on the optimum mass ratio

To derive the condition for optimum mass ratio, consider the case where the beam mass is fixed and only the mass of the tip mass is varied. The geometry of the tip mass and the beam is also fixed. It is analytically difficult to derive an explicit solution describing the optimum mass ratio. Hence, only two unique cases of significantly small and large *M* were considered. For situations where *M* is small, equation (53) can be written as equation (58) when the condition of optimum load resistance is met.

$$P_{max} \approx (\omega_1 Y_0 D_2 \varphi_0(L) F_1)^2 \frac{M}{32{\zeta_1}^2 {R_c}^2} \tag{58}$$

where

$$\varphi_0(L) = cosh\frac{\beta_n}{L}x - cos\frac{\beta_n}{L}x - \frac{O_{21}}{O_{22}}\left(sinh\frac{\beta_n}{L}x - sin\frac{\beta_n}{L}x\right) \tag{59}$$

The term $\omega_1$, $Y_0$, $D_2$, and $F_1$ are all dependent variables of the added mass. Substituting equation (20) into equation (48), the maximum critically damped stress term can be defined in terms of the natural frequency as

$$\sigma_i = \omega_1 h Y_0 D_2 F_1 \sqrt{\frac{Em}{LI}} \tag{60}$$

Substituting equation (60) into equation (58) and eliminating the constant terms,

$$P_{max} \propto \left(\frac{\sigma_i \varphi_0(L)}{\zeta_1}\right)^2 \tag{61}$$

If $\sigma_i$ and $\varphi_0(L)$ were plotted under a same variable, $\emptyset$, the following proportionality relation can be deduced

$$\sigma_i \propto \emptyset \tag{62}$$

$$\varphi_0(L) \propto \emptyset^{-0.5} \tag{63}$$

Multiplying equations (62) and (63) and squaring it to the power of two results in

$$\sigma_i \varphi_0(L) \propto \emptyset \tag{64}$$

This relation is identical to equation (62). Therefore, equation (61) can be simplified to

$$P_{max} \propto \frac{\sigma_i}{{\zeta_1}^2} \tag{65}$$

Substituting equation (50) into equation (65) leads to

$$P_{max} \propto \frac{\sigma_i}{[f(\sigma_i)+\zeta_h]^2} \tag{66}$$

where $A_1$, $A_2$ and $a$ defines the constant terms in the damping-stress equation. Now the thermoelastic damping term, $\zeta_h$, is a function of the beam's natural frequency and hence also a function of $\sigma_i$. The natural frequency of the beam can be related to the maximum critically damped stress by

$$\omega_1 = \frac{C_\sigma}{\sqrt{\sigma_i}} \tag{67}$$

where $C_\sigma$ is a constant. In this derivation, the thermoelastic damping equation from equation (37) was considered as it is easier to differentiate. Substituting equations (67) and (37) into equation (66) and differentiating results in

$$\frac{1}{{\zeta_1}^2} - \frac{1}{{\zeta_1}^3}\left[2\sigma_i f'(\sigma_i) - \zeta_h + \frac{{\zeta_h}^2}{\Delta e}\frac{C_\sigma}{\sqrt{\sigma_i}}\tau\right] \tag{68}$$

where $f'(\sigma_i)$ is the derivative of $f(\sigma_i)$ with respect to $\sigma_i$. To obtain the optimum condition, equation (67) must be equal to zero. Substituting equation (67) into equation (68) results in

$$\frac{1}{{\zeta_1}^2} - \frac{1}{{\zeta_1}^3}\left[2\sigma_i f'(\sigma_i) - \zeta_h + \frac{{\zeta_h}^2}{\Delta e}\omega_1\tau\right] = 0 \tag{69}$$

Rearranging equation (69) becomes

$$\zeta_1 + \zeta_h = 2\sigma_i f'(\sigma_i) + \frac{{\zeta_h}^2}{\Delta e}\omega_1\tau \tag{70}$$

It is difficult to relate $m_r$ to the parameters in equation (70) due to the boundary conditions and orthogonality consideration. However, Erturk and Inman [30] has pointed out that $m_r$ can be related to the frequency constant, $\beta_1$. The following approximation was derived for this relationship

$${\beta_1}^2 \approx \frac{1.6}{\sqrt{m_r}} \tag{71}$$

Substituting equation (71) into equation (70) results in

$$m_r \approx \frac{1.6Eh}{(\zeta_1+\zeta_h)L^2}\left[2Y_0 D_2 F_1 f'(\sigma_i) + \frac{{\zeta_h}^2\tau}{\Delta e\sqrt{12E\rho}}\right] \tag{72}$$

Therefore, ${m_r}^{opt}$ can be achieved when $m_r$ is equal to the right hand side of equation (72). Now considering the case where $M$ is significantly large, the condition of optimum load resistance is

$$P_{max} \approx 2m_e{\omega_1}^3(Y_0\varphi_1(L)F_1)^2\frac{1}{32\zeta_1} \tag{73}$$

Substituting in equation (71) and eliminating constant terms results in the following simplified proportionality

$$P_{max} \propto \frac{m_e \omega_1 \sigma_i}{\zeta_1} \tag{74}$$

Substituting in the damping-stress equation

$$P_{max} \propto \frac{m_e \omega_1 \sigma_i}{f(\sigma_i)+\zeta_h} \tag{75}$$

Since $m_e \omega_1$ increases when $\sigma_i$ increases, the function in equation (73) describes an infinitely increasing function. This suggest that for cases of large $M$, the power of the resonator will continually increase with increasing bulk mass and an optimum mass ratio does not exist. Figure 10 shows the variation of $P_{max}$ and $m_r$ for different values of $M$. The term ${m_r}^{est}$ in Figure 10 refers to the right hand side of equation (72).

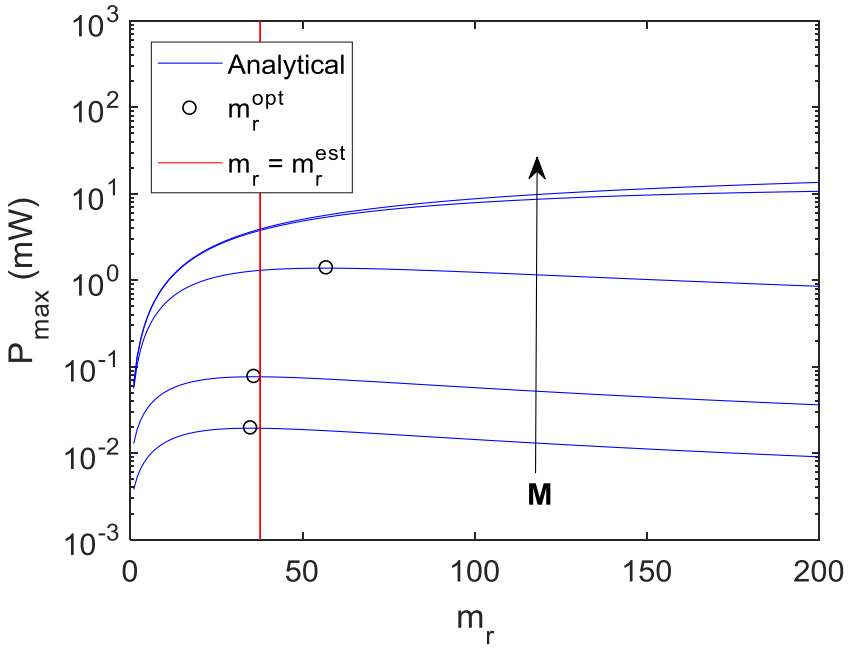


**Figure 10.** Optimum mass ratio under different $M$ values.

Figure 10 confirms the validity of equations (72) and (75). It is reminded that the optimum mass ratio condition derived here is only valid for cases when the geometry of the resonator is unchanged. In addition, the optimum conditions derived are based on the proposed damping-stress model and may not be valid if other damping-stress models are applied. Figure 11 analyses the effect of beam geometry on the optimum mass ratio. The optimum mass ratio was plotted against the cantilever beam's width and aspect ratio at four different $M$ values. The same base excitation acceleration was used in all of the analysis. The gaps in certain surfaces in Figure 11 represents regions where ${m_r}^{opt}$ does not exist.

Results in Figure 11 show that increasing $M$ and the aspect ratio results in an overall increase in the optimum mechanical damping ratio or the resonator. It is shown by the purple and yellow surfaces that when $M$ is high, there exist areas where ${m_r}^{opt}$ does not exist. This non-existent area is more dominant for beams with high aspect ratio and small width. This means that the range of $M$ where an optimum mass ratio exists is larger for beams with a low aspect ratio and large width. It is well aware that an optimum mass ratio also corresponds to a single natural frequency value, whereas in energy harvesting applications, tuning of the natural frequency is desired. However, the purpose of this subsection was to discuss on the effects of $M$ and the geometry of the beam on the value of the optimum mass ratio. In addition, knowing the optimum mass ratio will also give an insight on the range of natural frequencies where the resonator would be most efficient.

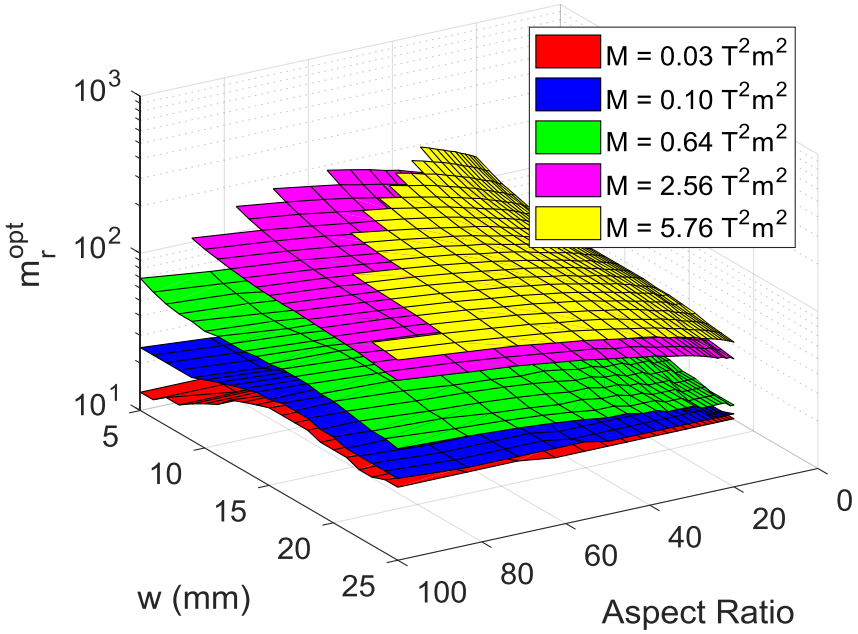


**Figure 11.** Variation in optimum mass ratio with beam geometry.

### 3.4 Tuning of natural frequency

In vibration energy harvester applications, the resonators are usually required to be tuned to a desired natural frequency to maximise its output performance. For cantilever beam-based applications, the most common manual frequency tuning methods are by changing the geometry of the beam (geometrical tuning) or by varying the mass of the tip mass (mass tuning). However, it is unclear as to which of the two methods would result in a better power output. Both methods are strongly dependent of the mechanical damping ratio parameter as any change in the beam's geometry and mass would result in a different damping capacity. Therefore, it is important that the variation in the mechanical damping of the beam is well defined before determining the preferable tuning method. Assuming a constant damping value would inevitably lead to erroneous predictions especially under large scale tuning. Figure 12 shows the variation in the natural frequency and maximum power output of a cantilever beam-based electromagnetic resonator for different beam aspect ratios at different $M$ values. A single curve in each subplot of Figure 12 represents a single aspect ratio that is tuned to a range of natural frequencies through mass tuning. The width of the beam was kept constant in this analysis. Note that each maximum power output displayed in Figure 12 corresponds to the condition of the optimum load resistance. The peaks in the curves of Figure 12 correspond to the optimum mass ratio.

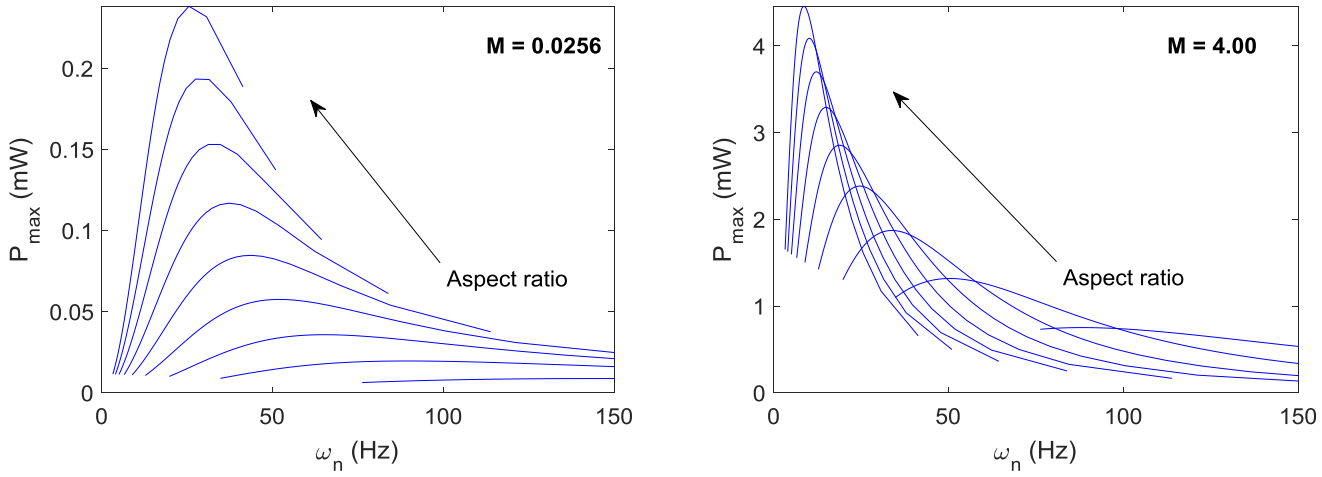

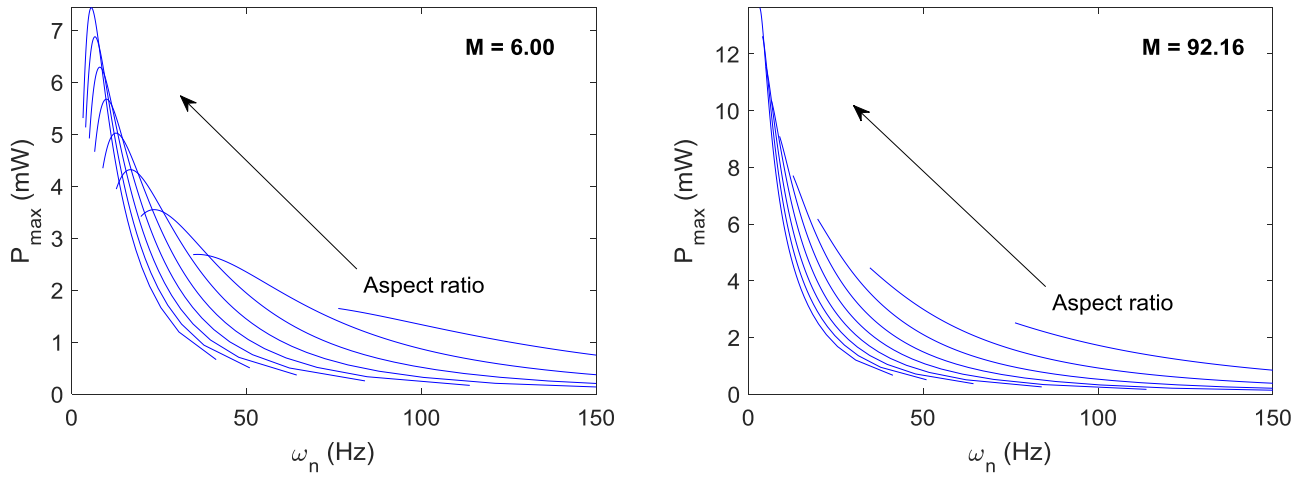


**Figure 12.** Variation of maximum power and natural frequency

Results in Figure 12 show that when *M* is very low, it is more desirable to select beams with a high aspect ratio prior to mass tuning the beam to the desired natural frequency. This is because a higher maximum power output was recorded for beams with a higher aspect ratio regardless of its natural frequency. Correspondingly, this also suggests that a lighter tip mass is preferable since increasing the aspect ratio of the beam decreases its natural frequency. As the value of *M* increases, the curves in Figure 12 shift to the left, reducing the optimum mass ratio. This results in a situation in where for each aspect ratio, there exist a certain limited range of natural frequencies in where the specific aspect ratio would perform better than other aspect ratios after mass tuning. When *M* is very high, it is observed that choosing a beam with a low aspect ratio prior to mass tuning now becomes more desirable. In addition, using heavier tip masses now becomes a preference as beams with a low aspect ratio would have a high natural frequency. It is worth to mention that no peaks are observed in the curves under high *M* values due to the reasons discussed in section 3.3. Overall, this analysis suggests that to maximise the power output of an electromagnetic resonator, it is better to maximise the aspect ratio of the resonator when dealing with low *M* values and maximise the mass of the tip mass at high *M* values. This also means that geometrical tuning takes priority at low *M* values and mass tuning is more beneficial at high *M* values. Figure 13 analyses the effect of three different beam widths on the power output of an electromagnetic harvester. The same *M* values and aspect ratios as in Figure 12 were used. The value of *w* in Figure 13 relates to the beam width used in Figure 12.

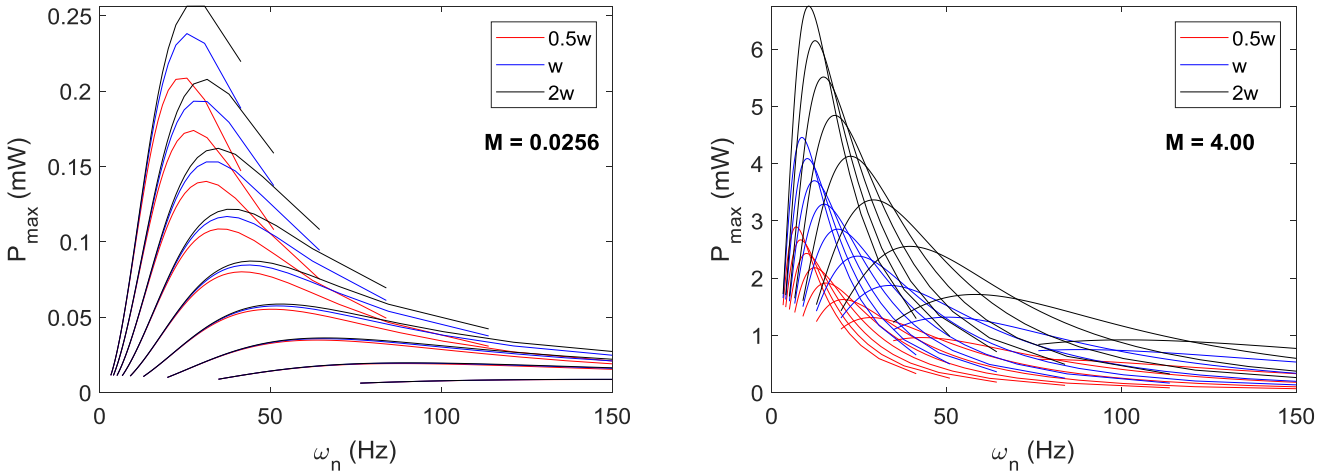

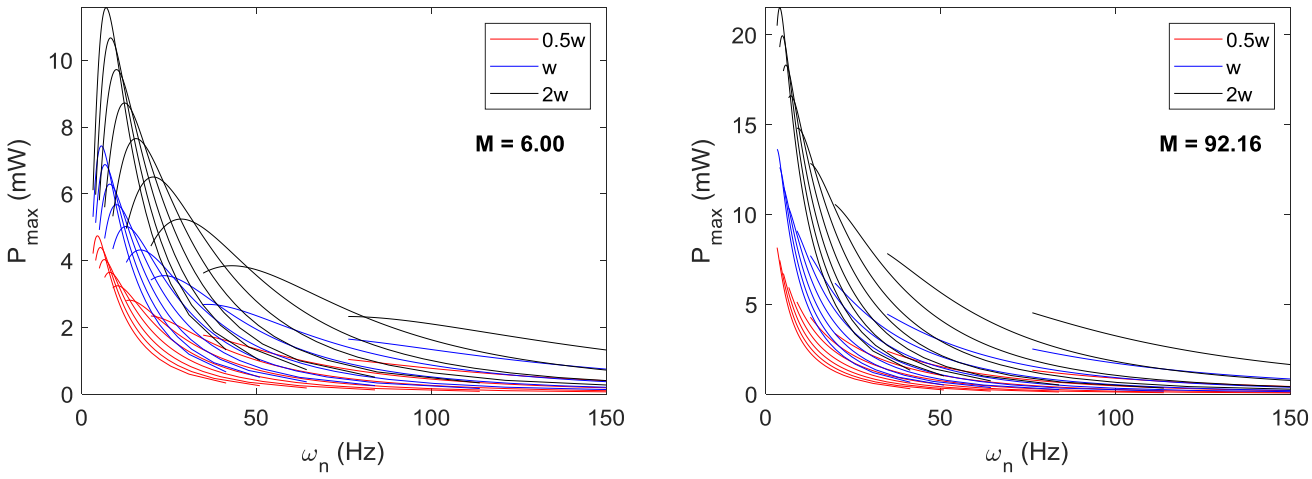


**Figure 13.** Variation in maximum power and natural frequency at different beam widths.

For all different $M$ values, a similar trend was recorded in Figure 13 for each aspect ratio in where the power output increases when wider beams are used. Table 2 summarises the results of this section on the type of parameters and tip mass to consider and preferable frequency tuning methods when optimizing an electromagnetic resonator for low and high $M$ values.

**Table 2.** Parametric considerations and preferable frequency tuning method for electromagnetic resonators.

| | High $M$ | Low $M$ |
|---|---|---|
| Beam aspect ratio | Low | High |
| Beam width | High | High |
| Mass of tip mass | High | Low |
| Preferred method for frequency tuning | Mass tuning | Geometrical tuning |

## 5. Conclusion

In this paper, the impact of mechanical damping on the performance of a cantilever beam-base electromagnetic resonator was analysed for macro scale volume. It was shown that for macro scale analysis, the material damping component is the major contributor to the total mechanical damping of the system as compared to thermoelastic damping and air damping. A new method was proposed to address the material damping of cantilever beams based on the critically damped stress parameter. This method is advantageous as compared to previous method in terms that the defined parameter is independent of the resonator's material damping. Therefore, the proposed method is simpler and more efficient to apply. In addition, this method can prove to be an effective approach for computer simulation applications. The proposed method can be applied to any material that resembles a non-complex hysteretic loop behaviour. An analysis was performed to study the implications of using a constant mechanical damping assumption on the power prediction of an electromagnetic resonator. Prior to that, the conditions for optimum load resistance of the resonator was derived. It was found that when the magnetisation parameter of the resonator is low, the optimum load resistance is equal to the coil resistance. However, when magnetisation parameter is significantly high, the optimum load resistance is determined when the mechanical damping ratio is equal to the electromagnetic damping ratio. Hence, this concludes the argument on the two commonly applied conditions of optimum load resistance.

A comparison was made between the analytical maximum power outputs using the developed mechanical damping model and the constant mechanical damping assumption. Results demonstrated different trends in both cases for certain set of parameters, leading to a large difference in the analytical prediction values between the two cases. In terms of maximum power output, the constant mechanical damping assumption demonstrated an increases in power output for an increases in the mass ratio of the resonator. On the other hand, the use of the mechanical damping model displayed a possible peak in the curve when plotted against its corresponding mass ratio under the optimised load resistance condition, which suggests that there exists an optimum mass ratio. The condition of the optimum mass ratio was derived for the cases of a small magnetisation parameter, whereas in cases of a large

magnetisation parameter, it was found that this optimum value did not exist. Knowing the optimum mass ratio of a resonator as it can provide an insight on the range of natural frequencies where the resonator would be most efficient. A final analysis was performed to determine the best manual tuning method for an electromagnetic resonator based on the developed mechanical damping model. It was found that under the conditions of low magnetization, it is preferable to geometrically tune the natural frequency of the resonator, whereas when high magnetisation is used, mass tuning the natural frequency would result in a higher power output. To summarise, the analysis presented in this work is only applicable for electromagnetic resonators. However, the proposed method to address the material damping of cantilever beams can be applied for any cantilever beam-based applications. Future works may look into the effect of time or number of vibrating cycles on the mechanical damping of a cantilever-beam based harvester. In addition, the study of mechanical damping in piezoelectric resonators will also be explored as a continuation to this work.

## References


[1] C.B. Williams, R.B. Yates, Analysis of a micro-electric generator for microsystems, Sens. Actuat. A. 52 (1996) 8–11.
[2] C.K. Thein, B.L. Ooi, J.S. Liu, J.M. Gilbert, Modelling and optimization of a bimorph piezoelectric cantilever beam in an energy harvesting application. J. Eng. Sci. Tech. 11(2) (2016) 212–227.
[3] K. Sang-Gook, S. Priya, I. Kanno, Piezoelectric MEMS for Energy Harvesting, MRS Bulletin 37.11. (2012) 1039–1050.
[4] S.P. Beeby, R.N Torah, M.J. Tudor, P. Glynne-Jones, T. O'Donnell, C.R. Saha, S. Roy, A micro electromagnetic generator for vibration energy harvesting, J. Micromech. Microeng. 17 (2007) 1257–1265.
[5] C. Wei, X Jing, A comprehensive review on vibration energy harvesting: Modelling and realization, Renew. Sustain Energy Rev. 74 (2017) 1–18.
[6] F. Qian, W. Zhou, S. Kaluvan, H. Zhang, L. Zuo, Theoretical modeling and experimental validation of a torsional piezoelectric vibration energy harvesting system, Smart Mater. Struct. 27 (2018) 045018.
[7] Y. Tan, Y. Dong, X. Wang, Review of MEMS Electromagnetic Vibration Energy Harvester, J. Microelectromech. Syst. 26(1) (2017) 1–16.
[8] B.L Ooi, J.M Gilbert, Design of wideband vibration-based electromagnetic generator by means of dual-resonator, Sens. Actuat. A. 213 (2014) 9–18.
[9] F. Goldschmidtboeing, P. Woias, Characterization of different beam shapes for piezoelectric energy harvesting, J. Micromech. Microeng. 18 (2008) 104013.
[10] J. Park, S. Lee, B.M. Kwak, Design optimization of piezoelectric energy harvester subject to tip excitation, J. Mech. Science Tech. 26(1) (2012) 137–143.
[11] S.J. Roundy, Energy Scavenging for Wireless Sensor Nodes with a Focus on Vibration to Electricity Conversion, Doctor of Philosophy Thesis (2003).
[12] R. Cruciat, C. Ghindea, Experimental determination of dynamic characteristics of structures, Math. Model. Civil. Eng. 4 (2012) 51–59.
[13] H. Nouira, E. Foltete, L. Hirsinger, S. Ballandras, Investigation of the effects of air on the dynamic behaviour of a small cantilever beam, J. Sound Vib. 305 (2007) 243–260.
[14] B.J. Lazan, Damping of materials and members in structural mechanics, London: Pergamon Press (1968).
[15] Y. Kume, F. Hashimoto, S. Maeda, Material damping of cantilever beams, J. Sound Vib. 80(1) (1982) 1–10.
[16] G.D. Gounaris, E. Antonakakis, C.A. Papadopoulos, Hysteretic damping of structures vibrating at resonance: An iterative complex eigensolution method based on damping–stress relation, Comp. Struct. 85 (2007) 1858–1868.
[17] F.M. Foong, C.K. Thein, B.L. Ooi, A.R. Abdul Aziz, Validation of Analytical Damping Ratio by Fatigue Stress Limit, IOP Conf. Ser.: Mater. Sci. Eng. 328 (2018) 012025.
[18] D. Edberg, Material damping of simple structures in a simulated space environment, J. Spacecraft Rockets 23(3) (1986) 288–296.
[19] C. Zener, W. Otis, R. Nuckolls, Internal friction in solids III: Experimental demonstration of thermoelastic internal friction, Phys. Rev. 53 (1938) 100–101.
[20] R. Lifshitz, M. L. Roukes, Thermoelastic Damping in Micro- and Nano-Mechanical Systems, Phys. Rev. B. 61(8) (2000) 5600–5609.
[21] Y. Sun, D. Fang, A.K. Soh, Thermoelastic damping in micro-beam resonators, Inter. J. Solids Struct. 43 (2006) 3213–3229.
[22] T.H. Metcalf, B.B. Pate, D.M. Photiadis, B.H. Houston, Thermoelastic damping in micromechanical resonators, App. Phys. Lett. 95 (2009) 061903.
[23] J.B. Alblas, A note on the theory of thermoelastic damping, J. Thermal Stress 4 (1981) 333–355.
[24] C. Zhang, G. Xu, Q. Jiang, Analysis of the Air-damping Effect on a Micromachined Beam Resonator, Math. Mechs. Solids 8(3) 2003 315–325.

[25] S.T. Chen, S. Du, E. Arroyo, Y. Jia, A. Seshi, Utilising Nonlinear Air Damping as a Soft Mechanical Stopper for MEMS Vibration Energy Harvesting, J. Phys: Conf. Ser. 773 (2016) 012098.
[26] W.E. Baker, W.E. Woolam, D. Young, Air and internal damping of thin cantilever beams, Inter. J. Mech. Sciences 9(11) (1967) 743–766.
[27] D.V. Iourtchenko, L. Duval, M.F. Dimentberg, On damping identification for certain SDOF systems, In: Developments in Theoretical and Applied Mechanics, Proc. SECAM XX Conf., 2000, Auburn, USA.
[28] M. Kim, M. Hoegen, J. Dugundji, B.L. Wardle, Modeling and experimental verification of proof mass effects on vibration energy harvester performance, Smart Mater. Struct. 19 (2010) 045023.
[29] N.E. Du Toit, Modeling and Design of a MEMS Piezoelectric Vibration Energy Harvester, Masters Thesis, 2005.
[30] A. Erturk, D.J. Inman, On mechanical modelling of cantilevered piezoelectric vibration energy harvesters', J. Intel. Mater. Syst. Struct. 19 (2007) 1311–1325.
[31] R.M. Lin, J. Zhu, On the relationship between viscous and hysteretic damping models and the importance of correct interpretation for system identification, J. Sound Vib. 325 (2009) 14–33.
[32] C. Zacharias, C. Konke, Experimental and Numerical Studies of Thermoelastic Damping, Proc. of the 7th GACM Colloquium on Computational Mechanics for Young Scientists from Academia and Industry, 2017, Stuttgart, Germany.
[33] R.F. Hu, Y.N. Deng, P. Li, Thermoelastic Damping in Microbeam Resonators with a Proof Mass, Adv. Mater. Res. 230–232 (2011) 1185–1189.
[34] A. Erturk, D.J. Inman, Issues in mathematical modelling of piezoelectric energy harvesters, Smart Mater. Struct. 17 (2008) 065016.
[35] H. Nouira, E. Foltete, B. Ait Brik, L. Hirsinger, S. Ballandra, Experimental characterization and modeling of microsliding on a small cantilever quartz beam, J. Sound Vib. 317 (2008) 30–49.
[36] J.L Dion, G. Chevallier, N. Peyret, Improvement of measurement techniques for damping induced by micro-sliding, Mech. Syst. Signal Process. 34 (2013) 106–115.
[37] F.M. Foong, C.K. Thein, B.L. Ooi, A.R. Abdul Aziz, A low-cost vibration analyser for analogue electromagnetic shaker, ICSIPA, 2017, Sarawak, Malaysia.
[38] B. Yang, C. Lee, W. Xiang, J. Xie1, J. Han He, R.K. Kotlanka, S.P. Low, H. Feng, Electromagnetic energy harvesting from vibrations of multiple frequencies, Micromech. Microeng. 19(3) (2009) 035001.
[39] C.T. Saha, T. O'Donell, H. Loder, S. Beeby, J. Tudor, Optimization of an electromagnetic energy harvesting device, IEEE Transactions on Magnetics 42(10) (2006) 3509–3511.